Level Alignment as Descriptor for Semiconductor/Catalyst Systems in Water Splitting: The Case of Hematite/Cobalt Hexacyanoferrate Photoanodes

Franziska Simone Hegner,[a] Drialys Cardenas-Morcoso,[b] Sixto Giménez,*[b] Núria López,*[a] and Jose Ramon Galan-Mascaros*[a, c]

The realization of artificial photosynthesis may depend on the efficient integration of photoactive semiconductors and catalysts to promote photoelectrochemical water splitting. Many efforts are currently devoted to the processing of multicomponent anodes and cathodes in the search for appropriate synergy between light absorbers and active catalysts. No single material appears to combine both features. Many experimental parameters are key to achieve the needed synergy between both systems, without clear protocols for success. Herein, we show how computational chemistry can shed some light on this cumbersome problem. DFT calculations are useful to predict adequate energy-level alignment for thermodynamically favored hole transfer. As proof of concept, we experimentally confirmed the limited performance enhancement in hematite photoanodes decorated with cobalt hexacyanoferrate as a competent water-oxidation catalyst. Computational methods describe the misalignment of their energy levels, which is the origin of this mismatch. Photoelectrochemical studies indicate that the catalyst exclusively shifts the hematite surface state to lower potentials, which therefore reduces the onset for water oxidation. Although kinetics will still depend on interface architecture, our simple theoretical approach may identify and predict plausible semiconductor/catalyst combinations, which will speed up experimental work towards promising photoelectrocatalytic systems.

Introduction

The production of solar fuels consists of harvesting sunlight as an energy source to transform a substrate into an energy-rich chemical through reduction. The reducing equivalents (electrons) are extracted from the complementary semireaction, in which another substrate (ideally water) gets oxidized. Hence, the efficiency and kinetics of the overall process undoubtedly depends on the latter, although the oxidation products typically have no commercial value. Without a fast and robust oxidation process, solar fuels will never reach market interests.

This is the reason why water-oxidation catalysis has become such a hot topic, as it is generally considered the major bottleneck towards the realization of artificial photosynthesis. Beyond electric potential requirements, water oxidation is a very slow process that includes a four-electron transfer and the chemically challenging formation of an oxygen–oxygen bond.

Several photoactive semiconductors possess appropriately aligned valence-band levels and a suitable band gap to drive water oxidation in their photoexcited state.[1] In this context, n-type metal-oxide semiconductor materials (e.g., TiO_2,[2] Fe_2O_3,[3] WO_3,[4] $BiVO_4$,[5] etc.) have been extensively studied as promising candidates to develop this technology, as they present relatively good stability under operation in harsh environments. From this family, α-Fe_2O_3 (hematite) is particularly appealing, not only because its favorable band gap of 1.9–2.2 eV allows for light absorption in the visible region but mainly because "rust" is one of the most abundant and cheap materials on earth.[3,6–9]

However, its application in photoelectrochemical water oxidation is severely limited owing to its unfavorable conduction band-edge level as well as its short carrier lifetimes and slow oxygen evolution kinetics.[8] Recombination in the bulk as a result of small polaron trapping impedes hole transport to the semiconductor–electrolyte interface,[10–12] whereas surface-state trapping causes electron–hole recombination before the oxidation reaction is able to proceed.[13–20]

To overcome the latter, that is, to enhance water-oxidation kinetics with respect to surface recombination, a common strategy is to modify the semiconductor surface with a water-oxidation catalyst (WOC).[9] An efficient hole-transfer catalyst

[a] *F. S. Hegner, Dr. N. López, Dr. J. R. Galan-Mascaros*
Institute of Chemical Research of Catalonia (ICIQ)
Av. Paisos Catalans, 16 Tarragona, 43007 (Spain)
E-mail: nlopez@iciq.es
jrgalan@iciq.es

[b] *D. Cardenas-Morcoso, Dr. S. Giménez*
Institute of Advanced Materials (INAM)
Universitat Jaume I
Castellon, 12006 (Spain)
E-mail: sjulia@uji.es

[c] *Dr. J. R. Galan-Mascaros*
ICREA
Pg. Lluís Companys, 23. Barcelona, 08010 (Spain)

Supporting Information and the ORCID identification number(s) for the author(s) of this article can be found under https://doi.org/10.1002/cssc.201701538.

on top of a photoactive semiconductor is thought to overcome the kinetic barriers of the sluggish water-oxidation reaction, which boosts the performance of the photoanode.[21,22] Consequently, the deposition of a stable and cost-effective WOC on a photoactive semiconductor material is crucial to achieve the targeted technoeconomical requirements.

Notwithstanding, the simple combination of such two systems does not guarantee success. Indeed, detailed studies on the mechanism of WOCs on iron-oxide photoanodes have pointed out that most "catalysts", although enhancing photoelectrochemical behavior, do not act as genuine catalysts, that is, they do not provide an effective hole-transfer pathway to increase the rate of water oxidation by lowering the activation barrier of the reaction. In many cases, the formation of the semiconductor/catalyst interface "only" increases the lifetime of surface recombination by acting as a capacitive layer or by passivating surface states.[20,23–25] A thick catalyst layer may even counteract photoelectrochemical activity by blocking light absorption or by inhibiting charge transport and ion diffusion from the electrolyte.[26,27] Moreover, an improvement in the photoelectrochemical (PEC) performance was also observed for noncatalytic overlayers, such as Al_2O_3 and Ga_2O_3, which either passivate surface states, as in the case of Ga_2O_3,[28–30] or change the energetic levels favorably, as in the case of Al_2O_3.[31]

The extent to which any semiconductor/catalyst combination has a chance of success can be predicted by computational methods, which in turn can save much time and efforts towards appropriate interface constructions.

We recently reported that cobalt hexacyanoferrate (CoFe-PB), a competitive WOC, acted preferentially as a genuine catalyst on top of photoactive $BiVO_4$ thin films.[32] Through DFT calculations, we assigned this behavior to favorable alignment of the energy levels, allowing CoFe-PB to participate as a viable bridge between the semiconductor and the water molecules. This synergy was experimentally assessed with CoFe-PB-decorated photoanodes, which exhibited a $+0.8$ V gain in photocurrent and a hole-extraction efficiency above 80%.[32]

Herein, we report the DFT analysis and experimental validation of a similar system, the hematite/CoFe-PB (Figure 1) composite photoanode. Computational models indicate that there is an intrinsic mismatch between these two materials, which implies that photoelectrocatalytic synergy should not occur. Indeed, our experiments are in excellent agreement with these predictions. CoFe-PB-decorated hematite electrodes show only a small improvement in photoelectrocatalytic water-oxidation activity that cannot be assigned to genuine catalytic behavior of CoFe-PB. Most probably, this is due to a surface-state shift that also shifts the water-oxidation onset to a lower potential. Such robust computational analysis will be very useful for any other semiconductor/catalyst ensemble by allowing for prior assessment of the validity of a proposed interface combination. These theoretical analyses will facilitate, and even push, future experimental research in the right direction towards final optimization of interfaces in photoelectrodes.

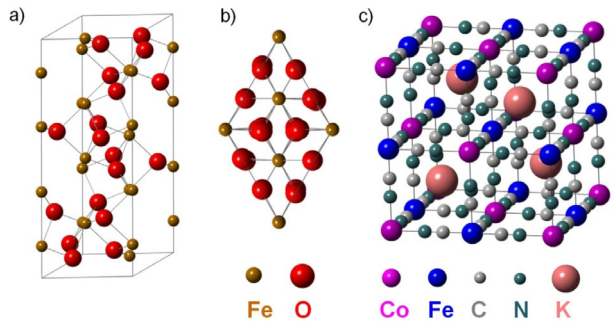

Figure 1. Representation of the crystal structures of a) the trigonal-hexagonal unit cell (space group $R\bar{3}6$), b) the predominant (0 0 1) surface facet (top view) of hematite (α-Fe_2O_3), and c) the cubic unit cell (space group $F\bar{4}3m$) of CoFe-PB ($KCo[Fe(CN)_6]$).

Results and Discussion

For efficient hole-transfer catalysis to occur, the catalyst needs to have its energy levels correctly aligned with the photoactive material, as schematized in Figure 2a for the case of the synergetic $BiVO_4$/CoFe-PB system.[32] In particular, this indicates that once the electron–hole pair is formed, the hole needs to be transferred to the catalyst; therefore, the corresponding levels in the catalyst need to be higher in energy than the valence band (VB) of the photoanode. This energy-alignment requisite is at the core of the process. If this thermodynamic condition is not fulfilled, as shown in Figure 2b, the "catalyst" will not exert efficient hole transfer.

Hybrid density functional theory (DFT) was used to calculate the electronic structures of α-Fe_2O_3, CoFe-PB ($KCo[Fe(CN)_6]$), and a solvated water molecule, as further described in the Experimental Section. Figure 2c shows the aligned densities of states (DOS) of the photoelectrochemical system: the hematite photoanode (left), the catalyst (middle), and water (right). To avoid confusion, it has to be noted that the calculated HOMO must not be mistaken with the electrochemical H_2O redox potential, although a linear relationship may exist.[33–35]

The calculated band gap of 1.95 eV for α-Fe_2O_3 matches well with its experimental value of 1.9–2.1 eV (Figure S6 in the Supporting Information).[6,7] This shows that the hybrid functional HSE03-13%, which includes 13% of exact exchange and which was previously optimized to match the electronic properties of CoFe-PB,[32] is also adequate to describe the electronic structure of α-Fe_2O_3 and follows previous indications by Pozun and Henkelman.[36] The VB edge of hematite consists of both O 2p and Fe 3d t_{2g} antibonding orbitals, which hybridize as a result of longitudinal lattice distortion along the main axis of the hexagonal unit cell (Figure 1). Hybridization of the strongly correlated Fe 3d levels and the bandlike O 2p levels in the VB was also found by photoemission studies and allows ligand-to-metal charge transfer by photoexcitation.[37,38] The distortion of the FeO_6 octahedra in the lattice also stabilizes the empty Fe d_{z^2} orbitals along the principal axis, which thus forms the conduction band (CB) minimum (together with a small Fe 4s contribution).

If a photon is absorbed, an electron of the O 2p VB will be excited to the Fe CB by a charge-transfer transition, as was

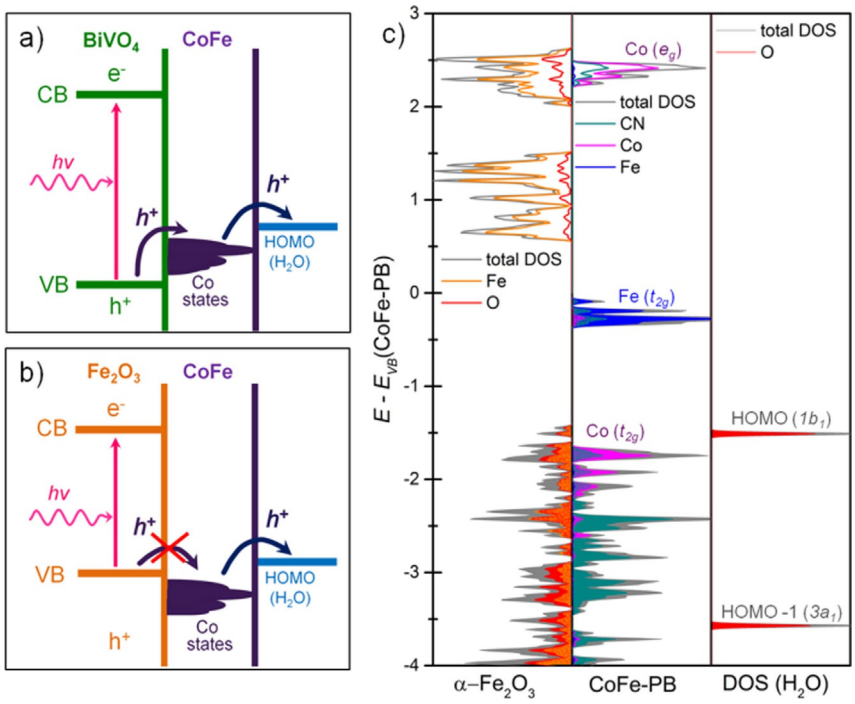

Figure 2. Energy-level alignment of a) a synergetic photoanode/catalyst interface: $BiVO_4$/CoFe-PB and b) a noncatalytic photoanode/catalyst combination: Fe_2O_3/CoFe-PB. c) Densities of states of α-Fe_2O_3 (left), $KCoFe[(CN)_6]$ (middle), and a solvated H_2O molecule (right) aligned by their O 2s bands. Filled electronic states are represented by filled areas. The CoFe-PB valence band edge is set as the zero energy level, that is, the given electronic levels do not coincide with electrochemical potentials, which are potential differences measured against a reference electrode.

seen in several X-ray photoemission and absorption studies, which hence leaves a hole in the VB that is then available for water oxidation.[37,39–41] The highest electronic state, that is, the highest occupied molecular orbital (HOMO), of water lies at the same energy (within the computational error of ± 0.1 eV) and, thus, is readily available to accept the hole at the Fe_2O_3 VB. From a thermodynamic viewpoint, disregarding kinetic effects and surface requirements, the hematite VB edge and the H_2O HOMO levels match adequately to induce electronic overlap, which is a necessary requirement for efficient electron (hole) transfer to take place. Nonetheless, small polaron effects and surface recombination prevent the efficient use of the hole.[10–20]

The CoFe-PB catalyst, however, has its filled Co d t_{2g} states, responsible for water oxidation,[32,42] slightly below the Fe_2O_3 VB edge (Figures 2b, c). Therefore, there is no thermodynamic driving force to favor hole transfer from Fe_2O_3 to CoFe-PB and, subsequently, to H_2O. This, in turn, does not mean that charge transfer to the catalyst will not occur. The Fe t_{2g} states, which lie approximately 1 V above the Fe_2O_3 VB, do not directly participate in the water-oxidation catalytic reaction, nor are they involved in the formation of the CoFe-PB/Fe_2O_3 interface. The strong CN binding from cyanide's C site makes the Fe centers inaccessible to coordination. Moreover, their electronic levels are far above the water HOMO, which excludes electronic overlap, required for water oxidation to occur. At finite temperatures and in an electrochemical environment, the CoFe-PB electronic levels, which lie close to the Fe_2O_3 VB, may accept/donate holes from/to Fe_2O_3/H_2O. All the same, the probability of CoFe-PB to have a true catalytic function, providing a faster hole-transfer pathway, on top of a hematite photoanode is negligible owing to level-alignment considerations. According to the DOS levels (Figure 2c), it is clear that there is an intrinsic mismatch, as the Co t_{2g} hole-acceptor level of CoFe-PB is at lower energy than the valence band of hematite. This indicates that hole transfer is neutral or slightly uphill and, thus, does not favor catalysis. Nevertheless, other beneficial effects of a CoFe-PB "catalyst" on hematite cannot be excluded. Tunneling[43] and hopping between sub-band-edge states within the barrier layer[44] have also been reported to describe charge transfer between photoactive and catalytic materials if the energy levels are not correctly aligned.

We also performed experiments to assess the validity of such a prediction. Nanostructured Zr-doped hematite films (see the Supporting Information for more details) were modified with the CoFe-PB catalyst by a sequential coating method at room temperature, as previously described.[32] The hematite electrode was submerged first in a ferricyanide solution and then in a cobalt chloride solution (both at neutral pH), which promoted the growth of the insoluble cobalt hexacyanoferrate. For our experiments, we generally used between three and six dipping cycles. Increasing the number of cycles did not significantly alter the photoelectrochemical performance of the photoanodes (as shown in Figure S3).

The electrodes were characterized by scanning electron microscopy (SEM) (Figure S4) and high-resolution transmission electron microscopy (HRTEM, Figure 3), both combined with energy-dispersive X-ray (EDX) spectroscopy. A total Fe/O ratio

of 32:68 is found, which is in good agreement with the Fe_2O_3 stoichiometry. More consistent evidence for the formation of Fe_2O_3 is provided by X-ray photoelectron spectroscopy (XPS) analysis (see Figure S5 and Table S2). The amount of the CoFe-PB catalyst is less than 1% and cannot be detected under SEM conditions. With HRTEM, however, cubic CoFe-PB crystallites can clearly be found on the Fe_2O_3 surface (Figure 3b, c). Their Co/Fe ratios are found to be between 50:50 and 60:40 by EDX spectroscopy, and they all lie in the stoichiometric possible range of 1:1 ($KCo[Fe(CN)_6]$) and 3:2 ($Co_3[Fe(CN)_6]_2$).[32,45,46] The presence of CoFe-PB on the surface is further confirmed by XPS, as described in the Supporting Information. Catalyst deposition does not show a significant influence on the optical UV/Vis absorption or band gap of the hematite semiconductor (Figure S6).

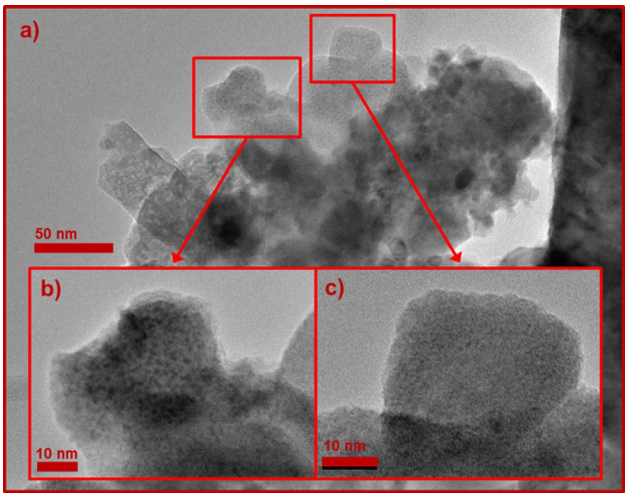

Figure 3. a) Electron micrographs obtained by HRTEM of a scratched CoFe-PB/α-Fe_2O_3 electrode with b, c) magnifications of the CoFe-PB crystallites found on the surface.

The photoelectrochemical behavior of the photoanodes was examined by cyclic voltammetry (CV) under chopped and constant illumination (Figure 4) in neutral (pH 7) potassium phosphate (KPi) buffer (0.1 M) solution. In the anodic scans at 50 mV s^{-1} (Figure 4a, c) an apparent cathodic shift in the photocurrent onset potential of 0.3 V can be seen. Nevertheless, scanning in the cathodic direction (Figure 4b) reveals a much smaller improvement in the photocurrent, which indicates that the apparent shift in the water-oxidation onset in the anodic direction is the result of the capacitive effect of the CoFe-PB layer, as the difference in anodic and cathodic scans for bare Fe_2O_3 is negligible. Indeed, scanning the CoFe-PB/α-Fe_2O_3 electrode at lower scan rates (Figures 4c and S7) significantly de-

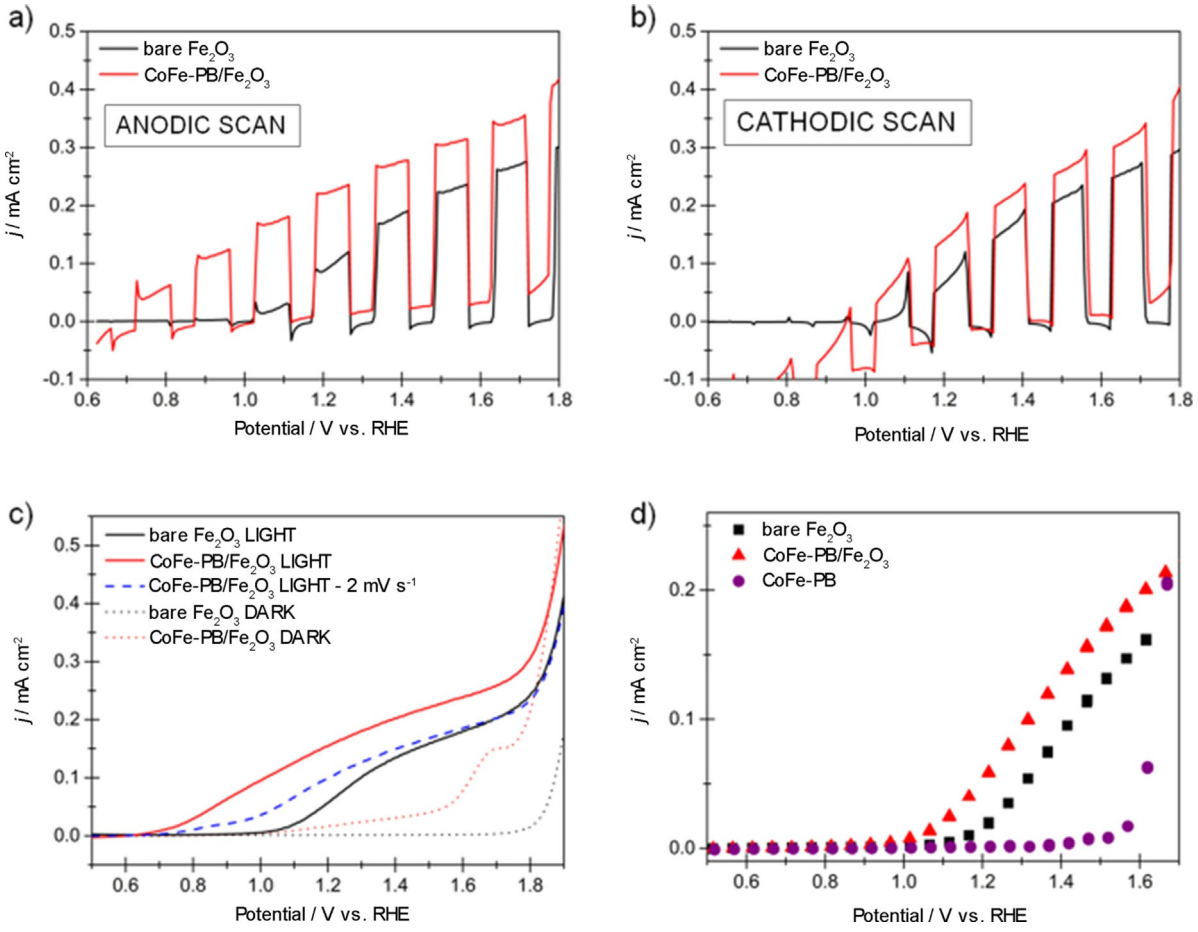

Figure 4. The *j*–*V* curves of CoFe-PB/Fe_2O_3 (red) and bare Fe_2O_3 (black) in 0.1 M KPi buffer solution at pH 7. a) Anodic and b) cathodic CV scans under chopped light (1 sun) at a scan rate of 50 mV s^{-1}. c) Anodic CV curve in the dark (dotted thin lines) and under light (thick solid lines) collected at scan rates of 50 (thick solid lines) and 2 mV s^{-1} (blue dashed line). d) Steady-state *j*–*V* curve extracted from the electrochemical impedance analysis data.

creases the observed photocurrent, whereas the scan rate barely affects the current density–voltage (*j–V*) behavior of bare hematite (Figure S7). Moreover, from the steady-state *j–V* curve (Figure 4d), which can be extracted from electrochemical impedance spectroscopy (EIS) analysis, as well as from scans at very low scan rates, the "real" photocurrent onset potential shift of 0.1 V can be determined. In here, the voltage needed to attain a photocurrent of 0.01 mA cm^{-2} was taken as the onset potential.

To gain mechanistic understanding of the effect of CoFe-PB on hematite photoelectrodes, PEC experiments were performed in the presence of hydrogen peroxide (0.5 M), which was found to be an optimal hole scavenger for hematite.[15] Under these conditions it is assumed that all holes that reach the surface will be rapidly injected into solution and no electron–hole recombination will take place at the semiconductor–liquid interface.[15] Figure 5a shows the photocurrents obtained with and without a hole scavenger under illumination at pH 7, and Figure 5b shows the calculated charge-transfer efficiencies as a function of applied potential (see Supporting Information for calculation details).

The measured CV curves in hole scavenger solution do not show significant differences, which implies that an equal number of holes reaches the semiconductor/electrolyte interface for both bare and CoFe-PB-modified hematite; thus, their charge-separation efficiencies are similar. This, in turn, implies that charge mobilities in the bulk and band bending are not affected by surface catalyst modification. Consequently, it can be safely claimed that surface modification of Fe_2O_3 by CoFe-PB does not alter its bulk properties. The photocurrent onset in hole scavenger, that is, without surface recombination, is equal to the flat band potential (V_{FB}) and is approximately 0.6 V versus reversible hydrogen electrode (RHE).[47]

The charge-transfer efficiency of CoFe-PB/Fe_2O_3 reaches its maximum at approximately 1.35 V versus RHE, whereas for bare Fe_2O_3 it is maximal at 1.57 V versus RHE. The magnitude of 60%, however, is equal for both bare and modified Fe_2O_3. This indicates that the CoFe-PB catalyst does not improve charge transfer to the electrolyte but that the catalyst shifts it to a lower potential, which is in line with the observed cathodic shift in the onset potential.

EIS measurements were performed to further investigate the effect of the catalyst layer on the photocurrent. The obtained Nyquist plots systematically show a single arc in the dark and, thus, were fit to a simple Randles' circuit,[48] whereas two arcs are obtained under illumination at high potential (see Figure S8). This is due to a different, indirect charge-transfer mechanism taking place, in which holes are trapped in surface states and are then transferred to the electrolyte.[17,23,49] It is apparent that the potential at which indirect charge transfer starts to occur is lower for CoFe-PB/Fe_2O_3 electrodes than for bare Fe_2O_3, as also described in the Supporting Information. These EIS data can be fit to a previously established equivalent circuit that accounts for indirect hole transfer via hematite surface states and that is shown in Figure 6a.[17,23,47,49] The equivalent circuit elements include the contact-dependent series resistance (R_S); the trapping resistance (R_{trap}) (Figure 6b), which describes trapping of charges into the surface state; the charge-transfer resistance (R_{CT}) from the surface state to the electrolyte (Figure 6b); the space-charge capacitance (C_{SC}) of the bulk semiconductor (Figure 6c); and the surface-state capacitance (C_{SS}) of the hematite surface traps (Figure 6d).

The resistances R_{trap} and R_{CT} (Figure 6a,b) are not influenced by the amount of catalyst on the surface. The trapping of holes into the surface state (described by R_{trap}) is not affected by the catalyst at all; this is in good agreement with the information provided by the experiments with the hole scavenger (Figure 5), for which no significant changes in the bulk properties of Fe_2O_3 are identified. On the other hand, hole transfer from the surface states occurs at lower potentials, in accordance with the cathodic shift of the onset potential (Figure 4) and the calculated charge-transfer efficiency (Figure 5).

The bulk capacitance of hematite C_{SC} (Figure 6c), which results from band bending in the space-charge region, seems to decrease slightly upon increasing the number of dipping cycles during deposition. This, however, can be attributed to having less Fe_2O_3 surface area exposed to the solution in the CoFe-PB/Fe_2O_3 anode as more CoFe-PB is added. With Mott–Schottky (MS) analysis (see the Supporting Information), the

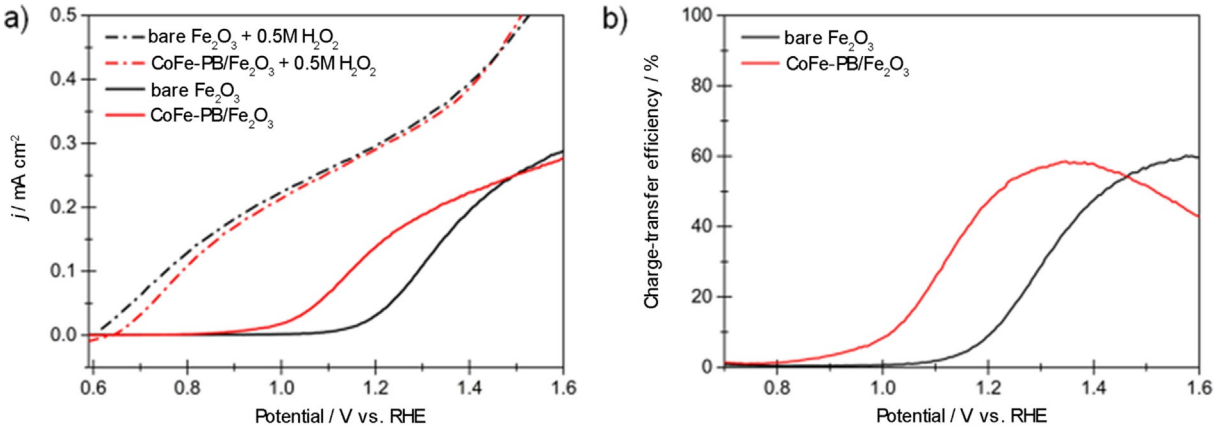

Figure 5. a) Anodic CV curves of CoFe-PB/ Fe_2O_3 (red) and bare Fe_2O_3 (black) in 0.1 M KPi buffer (solid lines) and 0.5 M H_2O_2 (dashed lines) solutions (both at pH 7) recorded at a slow scan rate of 2 mV s^{-1} to exclude catalytic, nonfaradaic current. b) Calculated charge-transfer efficiencies for both systems at pH 7.

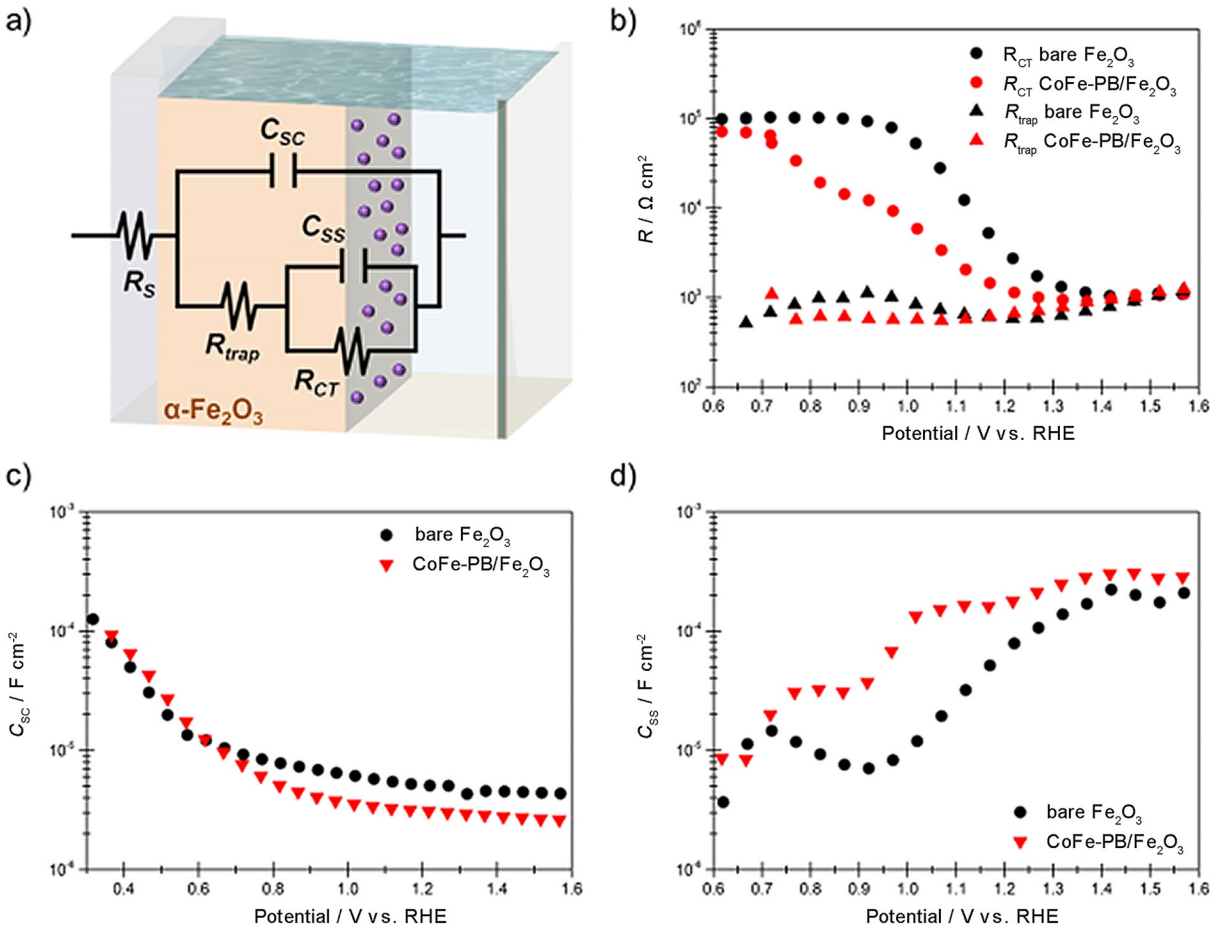

Figure 6. a) Equivalent circuit model used to fit EIS results obtained under 1 sun irradiation at higher potentials when indirect hole-transfer occurs. b) Charge-transfer (circles) and trapping (triangles) resistances of bare Fe_2O_3 (black) and CoFe-PB/Fe_2O_3 (red). c) Bulk and d) surface state capacitances of bare (black) and CoFe-PB coated (red) Fe_2O_3 semiconductor photoanodes. All spectra were obtained at pH 7 (0.1 M KPi buffer) and 1 sun irradiation.

flat band potential and the doping density of hematite were determined. As expected, the flat band potential, V_{FB} = (0.5 ± 0.05) V versus RHE, is independent of the CoFe-PB catalyst, which proves that CoFe-PB does not change the band positions. It differs by approximately 0.1 V from the photocurrent onset potential in the presence of a hole scavenger (which gives V_{FB} = 0.6 V vs. RHE) (Figure 5) owing to inaccuracies in the MS description for highly doped materials, as described by Zandi et al.[50] A flattening or horizontal shift in the MS curves, which was previously attributed to Fermi-level pinning,[17,23] is not observed here. The high annealing temperatures (800 °C) employed in this study are partially thought to passivate surface states and unpin the Fermi level, an effect that is also seen in the comparatively small photocurrent transients (Figure 3a,b).

Figure 6d shows the surface-state capacitance (C_{SS}) values of bare and CoFe-PB-modified hematite photoanodes. The magnitude of C_{SS} is not affected by CoFe-PB; hence, the "catalyst" does not passivate surface states. It can be seen clearly though, that the deposition of CoFe-PB shifts the surface state to lower potential. Hence, we conclude that the observed cathodic onset potential shift originates from shifting the surface state, which initiates indirect charge transfer through the surface states at a lower potential than for bare Fe_2O_3, and this, in turn, is due to oxidation of the CoFe-PB catalyst. A similar effect was found for Ga_2O_3 overlayers on hematite.[28] Furthermore, the trends followed by the two capacitances included in the model validate the selection of this equivalent circuit to fit our experimental results.

Although the energy-level alignment (Figure 2) does not favor hole transfer to the catalyst in its ground state, an applied external potential can initiate charge transfer to the catalyst in the surface, and this creates the oxidized $Co^{III}Fe^{III}$ states in CoFe-PB.[46,51] This transfer takes place at lower potentials than hole transfer to the surface state, which could also explain the cathodic shift in the surface-state capacitance.

Another important issue is related to the interfacial adhesion of Fe_2O_3 and the CoFe-PB catalyst. The larger the surface in contact between the photoanode and the catalyst, the more paths available for hole scavenging. As shown in a recent study by Shao-Horn et al., water wetting strongly influences the charge-transfer properties from/to the electrolyte/catalyst interface and, therefore, crucially determines the dynamics of the catalytic surface reaction.[52] A similar principle applies to the "wetting" of the catalyst on the semiconductor surface, which leads to hole transfer to the solution.

The micrographs in Figure 3 show that the nanoparticles are essentially nonwetting the oxide surface, which thus limits the

number of hole-transfer paths. The reasons behind the poor wetting can be traced back to the crystal structure of the compounds. The most common surface termination of hematite is hexagonal (Figure 1 b); however, the termination of PB is cubic, and this leads to lattice mismatch. Having incommensurate crystal facets minimizes the number of Co–O–Fe bridges at the interface, which are needed to enable hole transfer. Hence, catalyst "wetting" is another aspect that may be studied in silico and is linked to interface engineering that is crucial to its performance.

Conclusions

Light-harvesting semiconductors, which can transform sunlight into an electric-field potential as the driving force to produce fuels, are promising candidates for large-scale application of artificial photosynthesis technologies. However, they need to be coupled to an appropriate catalyst for the reaction to be efficient and fast enough. Generally, electron–hole recombination is faster than chemical transformations.

Beyond interfacial engineering requirements, there will be an important contribution from the correct alignment between the electronic levels from both the semiconductor and the catalyst. In this manuscript, we demonstrated how appropriate level alignment could be used to shed some light on possible charge-transfer pathways and, hence, to determine the applicability of a possible co-catalyst, as exemplified in the hematite/cobalt hexacyanoferrate case.

Although the applied DFT analysis used the simplified model of bulk structures only and did not include real electrochemical interfaces, it clearly showed that there was an intrinsic mismatch, as the catalyst hole-acceptor level was below the valence band of hematite in the energy diagram. Consequently, hole transfer to the catalyst was neutral or slightly uphill, and thus, there was no thermodynamic pathway for the generated holes in hematite to be transferred to the catalyst. This suggests that hole transfer to water, and thus water oxidation catalysis, is more likely to occur directly at the semiconductor surface. Nonetheless, different hole-transfer pathways, such as tunneling or hopping between sub-band-edge states, may be considered.[43,44] In good agreement, our experiments indicated that CoFe-PB decoration on top of hematite electrodes did not lead to a relevant enhancement in the photoelectrocatalytic performance. We assigned the small enhancement to longer lifetimes of electron–hole surface recombination as a result of the hole-scavenging character of the interface, which shifted the surface-state capacitance to more cathodic potentials. Water oxidation still preferentially occurred on the hematite surface as observed in different hematite/catalyst systems.[23,24] Therefore, the theoretical model of simple energy diagrams could predict the feasibility of this (and any other) junction. Interfaces may be engineered and improved, but if the process is thermodynamically uphill, their improvement is not due to an improvement in catalytic efficiency. For bare hematite in particular, finding a suitable true catalyst is a difficult task, as hematite has its valence band edge maximum very close to the HOMO of water. An appropriate co-catalyst would need to have filled electronic states between the valence band (VB) of Fe_2O_3 and the HOMO of H_2O, which are available for water oxidation (next to having accessible coordination sites). A better strategy could involve shifting the VB of Fe_2O_3 to lower energies, which could be achieved by suitable dopants[36] or surface modification with overlayers.[31]

In this line, analogous computational studies indicate that the favorable alignment of a photoactive semiconductor and catalyst (e.g., CoFe-PB/$BiVO_4$) leads to a remarkable increase in performance,[32] which corroborates the validity of our theoretical approach.

Experimental Section

Materials

Iron(II) chloride tetrahydrate ($FeCl_2{\cdot}4H_2O$, $>98\%$), zirconyl chloride octahydrate ($ZrOCl_2{\cdot}8H_2O$ $>99\%$), and potassium ferricyanide ($K_3[Fe(CN)_6]$, $\geq 99.0\%$) were purchased from Sigma–Aldrich, and cobalt chloride hexahydrate ($CoCl_2{\cdot}6H_2O$, $\geq 98.0\%$) was purchased from Fluka Analytical. Dimethyl sulfoxide (DMSO, $\geq 99.9\%$) and hydrogen peroxide solution [H_2O_2, 30% (*w/w*) in H_2O] were obtained from Sigma–Aldrich. The buffer solution was prepared from potassium phosphate monobasic and dibasic (KH_2PO_4, $\geq 99.0\%$; K_2HPO_4, $\geq 98.0\%$; Sigma-Aldrich). High-purity (Milli-Q) water was obtained with a Millipore purification system (Synergy) and was used for all solutions. Fluorine-doped tin oxide (FTO)-coated glass slides were purchased from Hartford glass (15 $\Omega\,cm^{-2}$).

Synthesis of hematite electrodes

Thin-film hematite electrodes were prepared by a simple and cost-efficient electrodeposition method, based on a description by Shaddad et al.,[53] but with varying calcination conditions as in Refs. [50,54]. Prior to deposition, FTO electrodes were ultrasonicated and then thoroughly cleaned with water and ethanol (isopropyl alcohol). Zr-doped metallic Fe was deposited from a solution of 20 mM $FeCl_2{\cdot}4H_2O$ and 0.9 mM $ZrOCl_2{\cdot}8H_2O$ in DMSO by applying a constant potential of -20. V vs. Ag/AgCl (3 M KCl) for 6 min. After carefully rinsing the films with Milli-Q water, the electrodes were calcined in air by heating up to 800 °C for 9–10 min, which was followed by rapid quenching at room temperature.

Sequential CoFe-PB coating

The CoFe-PB catalyst was deposited by sequentially dipping the hematite electrodes in reactant solutions of 0.02 M $K_3[Fe(CN)_6]$ in H_2O and 0.04 M $CoCl_2$ in H_2O, as we recently reported for $BiVO_4$ photoanodes.[32] First, the electrodes were dipped in $[Fe(CN)_6]^{3-}$ solution for 10–15 min with slow stirring, so that the negatively charged iron cyanide complexes could bind to the Fe_2O_3 surface. Afterwards, the electrodes were thoroughly rinsed with Milli-Q water and were then dipped in the Co^{2+} solution, again for 10–15 min with stirring to form CoFe-PB complex structures. The sequence was repeated at least two times to ensure significant CoFe-PB deposition. In all shown measurements, 3–6 repetitions were applied, which did not change the PEC behavior of the electrodes (see Figure S3 b).

Synthesis of CoFe-PB electrodes

For the sake of comparison, CoFe-PB/FTO electrodes were prepared by following the hydrothermal method described by Han et al.[42] In this method, CoO_x was first deposited by heating $Co(NO_3)_2$ and carbamide in an autoclave at 120° (10 h) and was afterwards derivatized to CoFe-PB in $K_3[Fe(CN)_6]$ solution at 60° (1–3 h).

Photoelectrochemical (PEC) measurements

PEC experiments were performed with an Eco Chemie Autolab potentiostat coupled with NOVA electrochemical software. A typical three-electrode cell consisted of the hematite photoanode as the working electrode, a Pt wire or mesh as the counterelectrode, and a Ag/AgCl (3 M KCl) reference electrode. All potentials were converted into the pH-independent reversible hydrogen electrode (RHE) by using the Nernst equation [Eq. (1)]:

$$V_{RHE} = V_{Ag/AgCl} + V^0_{Ag/AgCl} + 0.059 \cdot pH \quad \text{with } V^0_{Ag/AgCl}(3\ \text{M KCl}) = 0.21\ \text{V} \tag{1}$$

To normalize the measured current (in A) to a current density j in mA cm^{-2}, the electrode geometrical areas were determined by the graphical software ImageJ 1.50i. If not stated otherwise, the experiments were performed in a 0.1 M solution of potassium phosphate (KH_2PO_4) buffer at pH (7 ± 0.1). The pH was determined with a CRISON Basic 2° pH meter. Hole-scavenger experiments were performed in 0.5 M H_2O_2 solution (pH 7), which was described to be an effective hole scavenger by Warren et al.[15] A 450 W Xe arc lamp with an AM 1.5 solar filter (Sciencetech Inc.) was used to simulate sunlight of 100 mW cm^{-2} (1 sun). If not otherwise mentioned, cyclic voltammetry (CV) scans were typically performed at a scan rate of 50 mV s^{-1} until a stable signal was reached. For the CoFe-PB modified electrodes, approximately 2–3 CV scans were needed to stabilize the signal, but not for bare hematite. All hematite electrodes were illuminated from the electrolyte from the top of the hematite surface. This ensured a small mean free path for photogenerated holes, as hematite is well known to have very small hole-diffusion lengths between 2–4[55] and 20 nm.[56] Impedance data were collected between 10^{-1} and 40^6 Hz by using a 20 mV amplitude voltage perturbation and were analyzed with ZView software (Scribner associates). Steady-state j–V curves were extracted by monitoring the stabilized current at each applied voltage during the impedance measurement.

Structural and optical characterization

Morphologies, particle sizes, and chemical compositions were determined by scanning electron microscopy (SEM) with a JSM-7000F JEOL FEG-SEM system (Tokio, Japan) equipped with an INCA 400 Oxford EDX analyzer (Oxford, UK) and operating at 15 kV and a JEM-2100 JEOL transmission electron microscope operating at 200 kV that also contained an INCA 400 Oxford EDX analyzer (Oxford, UK). Prior to the SEM experiment, the samples were sputtered with a 2 nm thick layer of Pt. Surface analysis was performed by X-ray photoelectron spectroscopy (XPS) by using a Specs SAGE 150 instrument. The analyses were performed by using nonmonochromatic AlK_α irradiation (1486.6 eV) at 20 mA and 13 kV, a constant energy pass of 75 eV for overall analysis, 30 eV for analysis in the specific binding energy ranges of each element, and a measurement area of 1×1 mm^2. The pressure in the analysis chamber was 8×10^{-9} hPa. The data were evaluated by using Casa XPS software. The energy corrections of the spectra were performed considering a reference value of C 1s from the organic matter at 284.8 eV. UV/Vis spectra of the electrodes was recorded with a Cary 300 Bio spectrometer (UV0911M213). Absorbance and band gaps were calculated as described in the Supporting Information.

Computational details

Density functional theory (DFT) calculations were performed by using the Vienna Ab Initio Package (VASP)[57,58] on the model structures of stoichiometric $KCo[Fe(CN)_6]$ and α-Fe_2O_3 (Figure 1). Although real CoFe-PB is a nonstoichiometric compound, its electronic structure is not expected to vary from the ideal $KCo[Fe(CN)_6]$ structure.[59] However, a difference occurs owing to a change in the magnetic configuration, which is discussed in the Supporting Information. As pure density functional theory has proven insufficient to describe correctly the electronic structure of Prussian Blue type materials[60] and as DFT + U cannot unambiguously predict an explicit U-term needed to compare materials with different transition-metal centers,[60,61] a modified hybrid functional based on the HSE03 functional,[62,63] but including only 13% of exact Hartree–Fock (HF) exchange, was employed.[32] More information about the functional is given in the Supporting information. Projector Augmented Wave (PAW) pseudopotentials with small cores, expanding valence-subshell containing s and p electrons, ensured sufficient flexibility and were used for all metal atoms in the lattice.[64,65] For structure optimizations, a Γ-centered k-point mesh was used, and valence electrons were expanded in plane waves with kinetic energies up to 500 eV. Single-point calculations to obtain more accurate electronic structures were performed with a kinetic cutoff energy of 600 eV and denser Monkhorst–Pack k-point grids with $3 \times 3 \times 3$ (CoFe-PB) or $3 \times 3 \times 2$ (Fe_2O_3) k-points.[66] Water was calculated with the same scheme. For this, a single H_2O molecule in an asymmetric box (14.5 Å × 15 Å × 15.5 Å) was solvated through a continuum model. The implicit solvated water was represented through the MGCM method.[67,68]

All structures and calculations were uploaded to the ioChem-BD database, from which they are openly accessible.[69–71]

Acknowledgements

We would like to acknowledge financial support from the European Union (project ERC StG grant CHEMCOMP no 279313); the Spanish Ministerio de Economía y Competitividad (MINECO) through projects CTQ2015-71287-R, CTQ2015-68770-R and the Severo Ochoa Excellence Accreditation 2014–2018 SEV-2013-0319; the Generalitat de Catalunya (2014-SGR-797, 2014SGR-199 and the CERCA Programme); University Jaume I through the P11B2014-51 project; and the Generalitat Valenciana through the Santiago Grisolia Program, grant 2015-031. Serveis Centrals at UJI (SCIC) are also acknowledged. F.S.H. thanks the "LaCaixa"-Severo Ochoa International Programme (Programa internacional de Becas "LaCaixa"—Severo Ochoa) for a Ph.D. fellowship. We thank BSC-RES for generous computational resources.

Conflict of interest

The authors declare no conflict of interest.

Keywords: computational chemistry · electrochemistry · hematite · oxygen evolution catalysis · water splitting

[1] K. Sivula, R. van de Krol, *Nat. Rev. Mater.* **2016**, *1*, 15010.
[2] A. Fujishima, K. Honda, *Nature* **1972**, *238*, 37 – 38.
[3] K. L. Hardee, A. J. Bard, *J. Electrochem. Soc.* **1976**, *123*, 1024 – 1026.
[4] C. Fàbrega, S. Murcia-Lopez, D. Monllor-Satoca, J. D. Prades, M. D. Hernandez-Alonso, G. Panelas, J. R. Morante, T. Andreu, *Appl. Catal. B* **2016**, *189*, 133 – 140.
[5] T. W. Kim, K. S. Choi, *Science* **2014**, *343*, 990 – 994.
[6] J. H. Kennedy, K. W. Frese, *J. Electrochem. Soc.* **1978**, *125*, 709 – 714.
[7] R. M. Cornell, U. Schwertmann in *The Iron Oxides: Structure, Properties, Reactions, Occurrences and Uses, 2nd ed.*, Wiley-VCH, Weinheim, **2003**, pp. 9 – 38.
[8] K. Sivula, F. Le Formal, M. Grätzel, *ChemSusChem* **2011**, *4*, 432 – 449.
[9] A. G. Tamirat, J. Rick, A. A. Dubale, W.-N. Su, B.-J. Hwang, *Nanoscale Horiz.* **2016**, *1*, 243 – 267.
[10] S. M. Ahmed, J. Leduc, S. F. Haller, *J. Phys. Chem.* **1988**, *92*, 6655 – 6660.
[11] A. J. Bosman, H. J. Vandaal, *Adv. Phys.* **1970**, *19*, 1 – 117.
[12] L. M. Carneiro, S. C. Cushing, C. Liu, Y. Sude, P. Yang, A. P. Alivisatos, S. R. Leone, *Nat. Mater.* **2017**, *16*, 819 – 824.
[13] M. Barroso, S. R. Pendelbury, A. J. Cowan, J. R. Durrant, *Chem. Sci.* **2013**, *4*, 2724 – 2734.
[14] F. Le Formal, S. R. Pendlebury, M. Cornuz, S. D. Tilley, M. Grätzel, J. R. Durrant, *J. Am. Chem. Soc.* **2014**, *136*, 2564 – 2574.
[15] H. Dotan, K. Sivula, M. Grätzel, A. Rothschild, S. C. Warren, *Energy Environ. Sci.* **2011**, *4*, 958 – 964.
[16] B. Klahr, S. Gimenez, F. Fabregat-Santiago, T. Hamann, J. Bisquert, *J. Am. Chem. Soc.* **2012**, *134*, 4294 – 4302.
[17] B. Klahr, S. Gimenez, F. Fabregat-Santiago, J. Bisquert, T. Hamann, *Energy Environ. Sci.* **2012**, *5*, 7626 – 7636.
[18] B. Iandolo, A. Hellman, *Angew. Chem. Int. Ed.* **2014**, *53*, 13404 – 13408; *Angew. Chem.* **2014**, *126*, 13622 – 13626.
[19] N. Yatom, O. Neufeld, M. C. Toroker, *J. Phys. Chem. C* **2015**, *119*, 24789 – 24795.
[20] N. Yatom, Y. Elbaz, S. Navon, M. C. Toroker, *Phys. Chem. Chem. Phys.* **2017**, *19*, 17278 – 17286.
[21] F. Ning, M. Shao, S. Xu, Y. Fu, R. Zhang, M. Wei, D. G. Evans, X. Duan, *Energy Environ. Sci.* **2016**, *9*, 2633 – 2643.
[22] W. Liu, H. Liu, L. Dang, H. Zhang, X. Wu, B. Yang, Z. Li, X. Zhang, L. Lei, S. Jin, *Adv. Funct. Mater.* **2017**, *27*, 1603904.
[23] B. Klahr, S. Gimenez, F. Fabregat-Santiago, J. Bisquert, T. Hamann, *J. Am. Chem. Soc.* **2012**, *134*, 16693 – 16700.
[24] M. Barroso, A. J. Cowan, S. R. Pendelbury, M. Grätzel, D. R. Klug, J. R. Durrant, *J. Am. Chem. Soc.* **2011**, *133*, 14868 – 14871.
[25] L. Badia-Bou, E. Mas-Marza, P. Rodenas, E. M. Barea, F. Fabregat-Santiago, S. Gimenez, E. Peris, J. Bisquert, *J. Phys. Chem. C* **2013**, *117*, 3826 – 3833.
[26] D. K. Zhong, D. R. Gamelin, *J. Am. Chem. Soc.* **2010**, *132*, 4202 – 4207.
[27] G. Wang, Y. Ling, X. Lu, T. Zhai, F. Qian, Y. Tong, Y. Li, *Nanoscale* **2013**, *5*, 4129 – 4133.
[28] L. Steier, I. Herraiz-Cardona, S. Gimenez, F. Fabregat-Santiago, J.- Bisquert, S. D. Tilley, M. Grätzel, *Adv. Funct. Mater.* **2014**, *24*, 7681 – 7688.
[29] E. Aharon, M. C. Toroker, *Catal. Lett.* **2017**, *147*, 2077 – 2082.
[30] K. Ulman, M. T. Nguyen, N. Seriani, R. Gebauer, *J. Phys. Chem.* **2016**, *144*, 094701.
[31] O. Neufeld, N. Yatom, M. C. Toroker, *ACS Catal.* **2015**, *5*, 7237 – 7243.
[32] F. S. Hegner, I. Herraiz-Cardona, D. Cardenas-Morcoso, N. López, J. R. Galán-Mascarós, S. Gimenez, *ACS Appl. Mater. Interfaces* **2017**, DOI: 10.1021/acsami.7b09449.
[33] J. Conradie, *J. Phys. Conf. Ser.* **2015**, *633*, 012045.
[34] A. V. Marenich, J. Ho, M. L. Coote, C. J. Cramer, D. G. Truhlar, *Phys. Chem. Chem. Phys.* **2014**, *16*, 15068 – 15106.
[35] C. P. Kelly, C. J. Cramer, D. G. Truhlar, *J. Phys. Chem.* **2006**, *110*, 16066 – 16081.
[36] Z. D. Pozun, G. Henkelman, *J. Chem. Phys.* **2011**, *134*, 224706.
[37] A. Fujimori, M. Saeki, N. Kimizuka, M. Taniguchi, S. Suga, *Phys. Rev. B* **1986**, *34*, 7318 – 7328.
[38] M. Catti, D. Valerio, R. Dovesi, *Phys. Rev. B* **1995**, *51*, 7441 – 7450.
[39] G. Dräger, W. Czolbe, J. A. Leiro, *Phys. Rev. B* **1992**, *45*, 8283 – 8287.
[40] R. J. Lad, V. E. Henrich, *Phys. Rev. B* **1989**, *39*, 13478 – 13485.
[41] Y. Ma, P. D. Johnson, N. Wassdahl, J. Guo, P. Skytt, J. Nordgren, S. D. Kevan, J.-E. Rubensson, T. Böske, W. Eberhardt, *Phys. Rev. B* **1993**, *48*, 2109 – 2111.
[42] L. J. Han, P. Y. Tang, A. Reyes-Carmona, B. Rodriguez-Garcia, M. Torrens, J. R. Morante, J. Arbiol, J. R. Galan-Mascaros, *J. Am. Chem. Soc.* **2016**, *138*, 16037 – 16045.
[43] Y. W. Chen, J. D. Prange, S. Dühnen, Y. Park, M. Gunji, C. E. D. Chidsey, P. C. McIntyre, *Nat. Mater.* **2011**, *10*, 539 – 544.
[44] J. R. Avila, M. J. Katz, O. K. Farha, J. T. Hupp, *J. Phys. Chem. C* **2016**, *120*, 20922 – 20928.
[45] R. O. Lezna, R. Romagnoli, N. R. de Tacconi, K. Rajeshwar, *J. Phys. Chem. B* **2002**, *106*, 3612 – 3621.
[46] N. R. de Tacconi, K. Rajeshwar, R. O. Lezna, *Chem. Mater.* **2003**, *15*, 3046 – 3062.
[47] J. Bisquert, S. Gimenéz, L. Bertoluzzi, I. Herraiz-Cardona in *Photoelectrochemical Solar Fuel Production: From Basic Principles to Advanced Devices* (Eds.: S. Gimenéz, J. Bisquert), Springer International, Cham, Switzerland, **2016**, Chap. 6.
[48] J. E. B. Randles, *Discuss. Faraday Soc.* **1947**, *1*, 11 – 19.
[49] L. Bertoluzzi, P. Lopez-Varo, J. A. Jimenéz Tejada, J. Bisquert, *J. Mater. Chem. A* **2016**, *4*, 2873 – 2879.
[50] O. Zandi, A. R. Schon, H. Maihibabaei, T. W. Hamann, *Chem. Mater.* **2016**, *28*, 765 – 771.
[51] R. Martínez-García, M. Knobel, J. Balmaseda, H. Yee-Madeira, E. Reguera, *J. Phys. Chem. Solids* **2007**, *68*, 290 – 298.
[52] B. Han, K. A. Stoerzinger, V. Tileli, A. D. Gamalski, E. A. Stach, Y. Shao-Horn, *Nat. Mater.* **2017**, *16*, 121 – 126.
[53] M. N. Shaddad, M. A. Ghanem, A. M. Al-Mayouf, S. Gimenez, J. Bisquert, I. Herraiz-Cardona, *ChemSusChem* **2016**, *9*, 2779 – 2783.
[54] A. Annamalai, A. Subramanian, U. Kang, H. Park, S. H. Choi, J. S. Jang, *J. Phys. C* **2015**, *119*, 3810 – 3817.
[55] K. Sivula, R. Zboril, F. Le Formal, R. Robert, A. Weidenkaff, J. Tucek, J. Frydruch, M. Grätzel, *J. Am. Chem. Soc.* **2010**, *132*, 7436 – 7444.
[56] M. P. Dare-Edwards, J. B. Goodenough, A. Hemnett, P. R. Trevellick, *J. Chem. Soc. Faraday Trans. 1* **1983**, *79*, 2027 – 2041.
[57] J. Hafner, G. Kresse, *The Vienna Ab-Initio Simulation Program VASP: An Efficient and Versatile Tool for Studying the Structural, Dynamic, and Electronic Properties of Materials*, Plenum Press, New York, **1997**, pp. 69 – 82.
[58] G. Kresse, J. Furthmüller, *Phys. Rev. B* **1996**, *54*, 11169 – 11186.
[59] J. C. Wojdel, I. D. R. Moreira, S. T. Bromley, F. Illas, *J. Chem. Phys.* **2008**, *128*, 044713.
[60] F. S. Hegner, J. R. Galán-Mascarós, N. López, *Inorg. Chem.* **2016**, *55*, 12851 – 12862.
[61] M. Capdevila-Cortada, Z. Lodziana, N. Lopez, *ACS Catal.* **2016**, *6*, 8370 – 8379.
[62] J. Heyd, G. E. Scuseria, *J. Chem. Phys.* **2004**, *120*, 7274 – 7280.
[63] J. Heyd, G. E. Scuseria, M. Ernzerhof, *J. Chem. Phys.* **2003**, *118*, 8207 – 8215.
[64] P. E. Blöchl, *Phys. Rev. B* **1994**, *50*, 17953 – 17979.
[65] G. Kresse, D. Joubert, *Phys. Rev. B* **1999**, *59*, 1758 – 1775.
[66] H. J. Monkhorst, J. D. Pack, *Phys. Rev. B* **1976**, *13*, 5188 – 5192.
[67] M. Garcia-Ratés, N. López, *J. Chem. Theory Comput.* **2016**, *12*, 1331 – 1341.
[68] M. Garcia-Ratés, R. García-Muelas, N. López, *J. Phys. Chem. C* **2017**, *121*, 13803 – 13809.
[69] ioChem-BD software, http://www.iochem-bd.org/, Institute of Chemical Research of Catalonia (ICIQ), **2014**.
[70] M. Álvarez-Moreno, C. de Graaf, N. López, F. Maseras, J. M. Poblet, C. Bo, *J. Chem. Inf. Model.* **2015**, *55*, 95 – 103.
[71] F. S. Hegner, link to database: Photoanodes_Fe2O3_CoFe-PB, https://doi.org/10.19061/iochem-bd-1-51.